Numerical analysis of far-field fault reactivation induced by reservoir cooling

Ouf, Josselin; Vardon, Philip J.; Khaledi, Kavan; Luo, Wen; Jalali, Mohammadreza; Amann, Florian

DOI
10.1016/j.geothermics.2024.103234

Publication date
2025

Document Version
Final published version

Published in
Geothermics

Geothermics 127 (2025) 103234

Contents lists available at ScienceDirect

Geothermics

journal homepage: www.elsevier.com/locate/geothermics

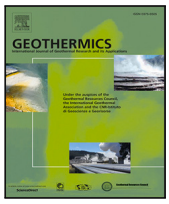

Numerical analysis of far-field fault reactivation induced by reservoir cooling

Josselin Ouf [a,b,*], Philip J. Vardon [b], Kavan Khaledi [a,c], Wen Luo [a,b], Mohammadreza Jalali [a], Florian Amann [a,c]

[a] Chair of Engineering Geology and Hydrogeology, RWTH Aachen, Aachen, 52064, Germany
[b] Faculty of Civil Engineering and Geosciences, Delft University of Technology, Delft, 2628 CN, The Netherlands
[c] Fraunhofer Institute for Energy Infrastructures and Geothermal Systems, Aachen, 52062, Germany

ARTICLE INFO

Keywords:
Hydrothermal system
Thermo-hydro-mechanics modeling
Numerical modeling
Coupled processes
Fault reactivation

ABSTRACT

This study presents a thermo-hydro-mechanical framework to model hydrothermal systems within a simplified faulted synthetic reservoir, replicating current production scenarios in The Netherlands and Germany. The reservoir, composed of porous and permeable sandstone, and the confining layer, made of porous but less permeable shale, undergoes a process where cold water is injected and hot water is extracted. A fault, situated 750 meters from the injection well, is investigated to examine the conditions when fault slip could occur. Various fault and formation stiffnesses are modeled to assess their impact on fault stability. Our analysis reveals that stress changes induced by hydrothermal operations can lead to fault reactivation, with the stiffness contrast between the reservoir and confining layers playing a significant role in when and where fault reactivation can occur. Stiffer confining layers lead to reactivation occurring more closely associated with the passage of the cooling front. In contrast, a stiffer reservoir results in greater and more gradual stress changes, making reactivation more closely related to the total volume of cooled rock.

1. Introduction

In hydrothermal systems, hot fluid is extracted at a production well, energy is then removed and the resulting colder fluid is reinjected via an injection well. This fluid circulation alters the initial pore pressure regime, impacting effective stress (Terzaghi, 1943; Skempton, 1954; Biot, 1955). Injection and extraction of a fluid also induce deformation of the solid skeleton of the rock that leads to changes in stress (Geertsma, 1957a; Zimmerman, 1990). As the cold fluid comes into contact with the hotter rock, the fluid absorbs energy from the rock, causing the rock to cool down (Tadmor et al., 2012; Zoback, 2010). The introduction of colder fluid from the injection well therefore causes the progression of a cooling front, primarily driven by advection (Cathles, 1977; Cathles III, 1990). This reservoir cooling leads to a change of stress and deformation within the reservoir (Geertsma, 1957b; McTigue, 1986). The resulting stress change has implications for fault stability. Depending on the fault orientation, the normal effective stress may decrease while the tangential stress increases, leading to an overall increase in fault instability (Jaeger et al., 2009; Zoback, 2010).

Upon fluid injection or extraction, the initial pore pressure is disturbed. During injection, the pore pressure near the well increases, leading to a pressure gradient that causes water to diffuse away from the well (Zoback, 2010). During extraction, the pore pressure near the well decreases, resulting in a pressure gradient that causes water to flow towards the well (Dake, 1983). After fluid is injected or extracted from the rock matrix, the pore volume changes due to the (de)pressurized water occupying the pore space (Zimmerman, 1986; Chilingarian and Wolf, 1975). The increase or decrease in volumetric stress caused by poroelastic effects progresses more extensively and rapidly compared to the spread of pore pressure during injection, as shown by e.g. Duboeuf et al. (2021), Krietsch et al. (2020), Boyet et al. (2023). This poroelastic phenomenon, induced by fluid injection or extraction imposing respectively tensile or compressive stress increments, has the potential to either enhance or diminish fault stability based on their orientations (Segall and Lu, 2015; Zaal et al., 2021). The advancement of the cooling front in the reservoir exhibits less prominence in spatial distribution and is observed to propagate at a slower rate compared to the effects of poroelasticity and fluid propagation, as demonstrated by Jeanne et al. (2014) and Blöcher et al. (2018).

Changes in pore pressure and temperature can jeopardize the stability of faults (Geertsma, 1957b; Lord and Shulman, 1967). This phenomenon can be illustrated by a Mohr–Coulomb failure envelope, where stress states are represented by Mohr's circle (see Fig. 1). Injection activities lead to an increase in fluid pressure (Dake, 1983). Subsequent cooling of the reservoir causes contraction, reducing horizontal stresses due to geometric constraints, while vertical effective

* Corresponding author at: Chair of Engineering Geology and Hydrogeology, RWTH Aachen, Aachen, 52064, Germany.
E-mail address: j.ouf@tudelft.nl (J. Ouf).

https://doi.org/10.1016/j.geothermics.2024.103234
Received 23 July 2024; Received in revised form 27 November 2024; Accepted 4 December 2024
Available online 8 January 2025

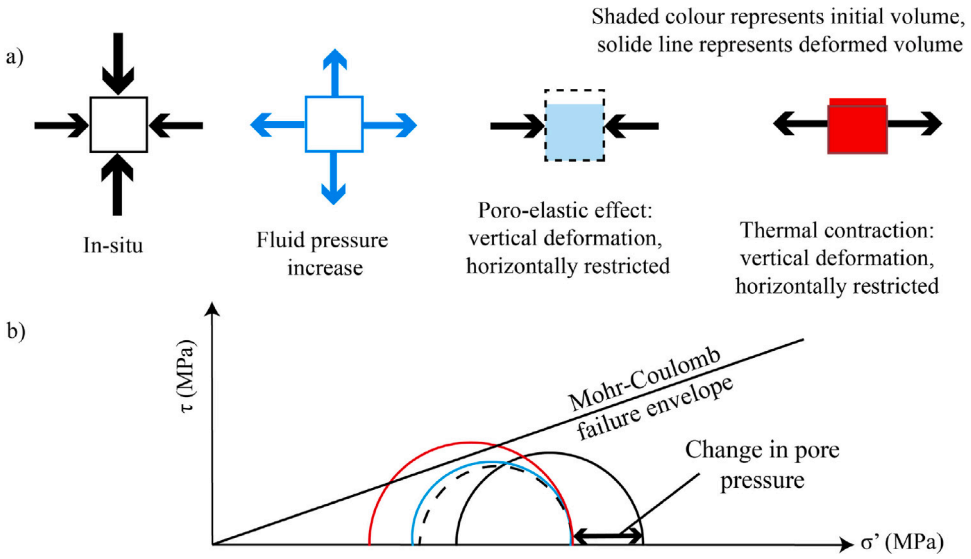

Fig. 1. Diagram illustrating stress changes in a geothermal reservoir (Vardon (2024) - Personal Communication): (A) Components contributing to the final stress state; (B) Mohr's circle and failure envelope demonstrating thermo-hydro-mechanical stress alterations. Line colors/types in (A) correspond to Mohr's circles in (B).

stress remains unaffected by thermal effects, offset by overburden pressure (Cryer, 1963; Mandel, 1953). A fault nearing or reaching its failure threshold under stress conditions is considered critically stressed, indicating potential for seismic activity (Jaeger et al., 2009; McClure and Horne, 2014; Buijze et al., 2019). Slip is predicted to arise when Mohr's circle is predicted to intersect or exceed the failure envelope, as shown in Fig. 1.

Seismicity has been observed to occur after pore pressures have stabilized, pointing to other triggering mechanisms such as the thermal effects (Kivi et al., 2022; Buijze et al., 2023). Noteworthy events with magnitudes $M_L \geq 2$ in Unterhaching (Germany) were observed within a few months to three years after pore pressure stabilization, suggesting cooling as a triggering factor (Megies and Wassermann, 2014). Similarly, in Poing (Germany), two events with $M_L \geq 2$ occurred five years post-circulation commencement, indicating again cooling as a potential trigger as pore pressures would have been stable long before then (Seithel et al., 2019). Moreover, in the Californië geothermal field in the Netherlands, cooling of the fractured carbonates reservoir induced events with a magnitude (M_L) of 1.7. This led to the suspension of the Dutch project due to concerns related to induced seismicity (Voros and Baisch, 2022).

Numerical modeling can enhance the comprehension of the impact of stress changes within cooling reservoirs, arising from alterations in pore pressure and temperature (Rutqvist and Tsang, 2002; Rutqvist et al., 2013). In a study conducted by Jacquey et al. (2015), the analysis of a synthetic case revealed that a fault situated between an injector and a producer well predominantly experiences slipping due to thermal effects rather than pore pressure effects. In a numerical poro-thermo-elasticity study conducted by Jacquey et al. (2016), the investigation focused on assessing the influence of pore pressure and temperature changes on the stability of the fault at the GroßSchönebeck geothermal site. The study underscored the significance of coupling these factors in numerical simulations (Jacquey et al., 2016). Furthermore, in a 2D synthetic model, Kivi et al. (2022) demonstrated that faults located 1 km away from the injector and producer can undergo reactivation primarily due to thermal effects. In this scenario, the stress change at the fault was a result of reservoir contraction elsewhere in the system, as the cooling front does not reach the fault (Kivi et al., 2022).

From a modeling prespective, fractures can be implicitly represented using an equivalent porous media approach. Prominent codes that utilize this method include OpenGeoSys (Kolditz et al., 2012), the MOOSE framework (Permann et al., 2020), TOUGH-FLAC (Itasca, 2011; Rutqvist, 2017), and CODE_BRIGHT (Olivella et al., 1996). Conversely, the explicit representation of fractures aims to realistically capture the geometry and impact of fractures, often requiring specialized treatment. Notable techniques for explicit fracture modeling include FEM-DEM/cohesive zone modeling (Lisjak et al., 2014; Grasselli et al., 2015), Discrete Fracture Network using interface elements (Gischig and Preisig, 2015), and Embedded lower-dimensional elements (Watanabe et al., 2012). In this work we use a continuous FEM approach, with a fracture zone that incorporate a zero-thickness element to replicate the fracture.

The current study aims to develop a numerical model for a synthetic geothermal project in a sandstone hydrothermal reservoir. The reservoir includes a fault zone located at 750 m away from the injection point. The reservoir properties and the depiction of the heat extraction scenario draw inspiration from the comparative analysis presented in Buijze et al. (2023) and the Tiefe Geothermie 2023/24 project in Germany (Piesnack, 2023). These detail current hydrothermal projects, including reservoir properties and injection scenarios, and discuss fault stability (Buijze et al., 2023; Piesnack, 2023). Our modeling approach integrates a coupled poro-thermo-hydro-mechanics framework, including key couplings.

The critical parameters for fault reactivation need to be investigated to identify cases where faults are more prone to reactivation (Rutqvist et al., 2013; Kivi et al., 2022), and to investigate how reactivation evolves. To address this issue, this study investigates and quantifies the impact of fault, reservoir and caprock stiffness.

The primary focus is on investigating the potential reactivation of a fault situated 750 meters away from the injection well. The specific objectives include:

- Assessing the slip tendency of a fault located at a 750 m away from the injection well.
- Investigating the triggering mechanism, considering poro-thermo-hydro-mechanics.
- Sensitivity analysis of the system by examining the effects of varying stiffness properties.
- Evaluating the propagation of ruptured area.

By addressing these objectives, our study seeks to provide an insight of fault behavior in a hydrothermal reservoir.

2. Modeling approach

2.1. Fully coupled numerical simulator

In our investigation, the PorousFlow and TensorMechanics modules within the MOOSE framework, developed by the Idaho National Laboratories, were used to construct our numerical model (Permann et al., 2020; Wilkins et al., 2020, 2021). MOOSE makes use of advanced mesh libraries such as libMesh to enable parallel computations with adaptive mesh refinement (AMR) (Kirk et al., 2006). It also leverages PETSc to achieve scalable solutions for scientific applications that involve partial differential equations in a parallel computing environment (Balay et al., 2017). Previously, the MOOSE framework, in conjunction with the GOLEM application (Cacace and Jacquey, 2017), was utilized by Jacquey et al. (2018) to simulate hydraulic stimulation at the Geothermal Site of GroßSchönebeck. Moreover, Sheldon et al. (2021) employed MOOSE with PorousFlow module to investigate the thermo-hydraulics of an aquifer thermal energy storage system. Additionally, Smith et al. (2022) utilized MOOSE with PorousFlow module to calculate permeability of fractures and its implications for geothermal fluid flow and the influence of seismic-scale faults.

2.2. Coupled thermo-hydro-mechanical equations

2.2.1. Mechanical formulation

The momentum balance, neglecting inertial effects, can be written as (Tadmor et al., 2012; Wood, 2017):

$$\nabla \cdot \boldsymbol{\sigma}' - \rho g = 0 \tag{1}$$

where $\boldsymbol{\sigma}'$ is the effective stress tensor, ρ the density and g the acceleration.

The effective stress $\boldsymbol{\sigma}'$ in Eq. (1), incorporating both hydraulic and thermal components, can be calculated as follows (Tadmor et al., 2012; Wood, 2017):

$$\Delta\boldsymbol{\sigma}' = \mathbb{C} : \Delta(\boldsymbol{\varepsilon}_{\mathbf{mechanical}} - \boldsymbol{\varepsilon}_{\mathbf{thermal}}) - \alpha_b \Delta p_f \boldsymbol{I} \tag{2}$$

where $\mathbb{C}$ is a tensor incorporating the constitutive behavior, $\boldsymbol{\varepsilon}$ is the strain tensor (small strain assumption), α_b is the Biot coefficient, p_f is the pore pressure and $\boldsymbol{I}$ is the identity tensor.

Shear failure induced dilation is represented by the dilation angle, ψ, which controls the magnitude of the volumetric strain during plastic deformation. The Mohr–Coulomb plastic strain is generally defined as follows (Wood, 2017):

$$\epsilon^p = \lambda \frac{\partial g_p}{\partial \sigma} \tag{3}$$

where, ϵ^p is the plastic strain, λ is the lagrange multiplier and g_p the plastic flow potential. The plastic flow potential in Mohr–Coulomb is generally defined as (Wood, 2017):

$$g_p = \tan\psi \ \sigma'_n + c \tag{4}$$

where, τ is the shear stress and σ'_n is the effective normal stress on the fracture plane. The parameters ψ and c are the dilation angle and the cohesion, respectively.

2.2.2. Hydraulic formulation

The equation for the mass balance of liquids in a porous medium is generally defined as (Pruess et al., 1999):

$$\frac{\partial n\ \rho_f}{\partial t} + n\ \rho_f \frac{\partial \varepsilon_{vol}}{\partial t} = -\nabla \cdot \boldsymbol{q}_f + q^*, \tag{5}$$

where q^* is the source term (injection), n the porosity, ρ_f fluid density. The term ε_{vol} is the volumetric strain, which is a coupling term showing the effect of mechanical deformation on the water pressure.

The generalized Darcy's law (Darcy, 1856) was used to describe the flow velocity of water $\boldsymbol{q}_f$ in Eq. (5) (neglecting gravitational pressure gradient):

$$\boldsymbol{q}_f = -\rho_f \frac{\boldsymbol{k}}{\mu_f}(\boldsymbol{\nabla} p_f + \rho_f \boldsymbol{g}) \tag{6}$$

where μ_f is the dynamic viscosity of water, $\boldsymbol{k}$ is the intrinsic permeability tensor of the medium and $\boldsymbol{g}$ is the acceleration

2.2.3. Thermal formulation

The equation for the energy balance of in a porous medium is (Pruess et al., 1999):

$$\frac{\partial \boldsymbol{\xi}}{\partial t} + \boldsymbol{\xi} \frac{\partial \varepsilon_{vol}}{\partial t} = -\nabla \cdot \boldsymbol{F}^T + q^T \tag{7}$$

where ε_{vol} is the volumetric strain of the bulk, $\boldsymbol{\xi}$ is the thermal energy per unit volume in the rock-fluid system, $\boldsymbol{F}^T$ the heat flux, q^T the heat forcing term (injection/production).

The thermal energy per unit volume in the rock-fluid system, $\boldsymbol{\xi}$ in Eq. (7) is expressed as (Pruess et al., 1999):

$$\boldsymbol{\xi} = (1-n)\rho_r C_r T + n\rho_f C_f T \tag{8}$$

where ρ_r is the density of the rock, C_r is the volumetric heat capacity of the rock, T temperature, ρ_f density of the fluid, C_f volumetric heat capacity of the fluid.

The heat flux equation in Eq. (7) is as follow (Pruess et al., 1999):

$$\boldsymbol{F}^T = \boldsymbol{q}_f h + \lambda \nabla T \tag{9}$$

where h is the enthalpy of the liquid phase and λ is the thermal conductivity, the bulk thermal conductivity is three times the linear thermal conductivity.

2.3. Model set up

The domain, measuring 6500 m x 6500 m x 800 m, encompasses the fracture zone, reservoir, and confining layer, as illustrated in Fig. 2. The model includes two confining layers, each 300 meters thick, which confine a 200 meter thick reservoir. A fault is included in the model, and is represented by a zero-thickness element within a 20m-wide fault zone. This fault is inclined at a 60 degree angle between the Z and X axes and has an offset of 30 m. The center of the fault is positioned at the X coordinate of 2590 m and the fault runs parallel to the Y axis (Fig. 2). The injection well is located at a distance of 750 meters along the X coordinate from the fault and Y = 3250 m. This well is modeled as a 1D line with a length of 180 m perpendicular to the Z axis, with the lowest point being 10 m from the bottom of the reservoir. The production well is situated 1600 m away from the injection well. As for the injection well, it is modeled as a 1D line, 180 m in length in the direction of the Z axis, and again the lowest point is 10 m from the reservoir's bottom. The well to well distance aims to prevent rapid thermal breakthrough and maximize the project's lifespan. In all simulations, a constant injection and flow rate of 150 l/s was utilized, with the fluid introduced at a temperature of 30 °C. The producer extracts fluid at a matching flow rate of 150 l/s. Around 50 years of production is simulated. This scenario is typical of Dutch and German projects (Buijze et al., 2019; Piesnack, 2023). This paper presents models of four different scenarios, each representing varying levels of stiffnesses for different materials in the domain. Detailed material properties can be found in Tables 1–3.

The reservoir is considered to be composed of sandstone and characterized by properties inspired by Buijze et al. (2023). Hydraulically, the reservoir is considered to be a permeable porous medium, governed by Darcy's law. The thermal aspect encompasses conduction and fluid heat advection. Mechanically, the sandstone reservoir is considered to adhere to Hooke's law, i.e. it is perfectly linearly elastic. The confining layer represents a shale, which is a porous medium with low permeability, that follows Darcy's law, and thermal behavior considers both conduction and fluid advection. Mechanically, the confining layers are linear elastic, i.e. adhere to Hooke's law. The fault zone is modeled

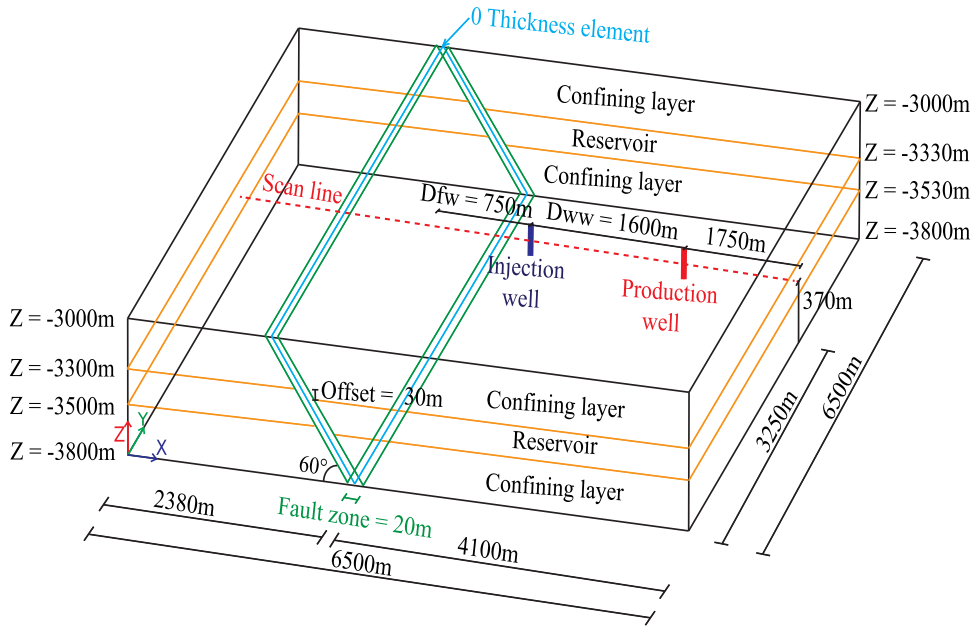

Fig. 2. Model domain and geometry.

with the Mohr–Coulomb constitutive model (Eqs. (3) and (4)). The relevant properties are detailed in Table 1, which were chosen to be representative of field conditions (Buijze et al., 2023). The fault zone hydraulically is modeled as a 2D element embedded in a 3D permeable porous medium, governed by Darcy's law, with heat transport again including both conduction and fluid advection. Within this fault zone, a zero-thickness element (2D) is employed to allow the influence of a realistic fault aperture on the hydraulic properties. The permeability for the zero-thickness element is represented by an equivalent transmissivity, calculated as: T = k · a, k represents the permeability of the fault (m^2), a signifies the fault aperture (m). The transmissivity T has units of (m^3) (or equivalently $m^2 \cdot m$), reflecting the product of permeability and aperture. Similarly, the porosity is expressed as a 3D equivalent, denoted as $n_{0thickness} = n \cdot a$, where a is the fault aperture, and n represents the fault porosity. A constant aperture has been assumed, set at 1.1 micrometers. Consequently, $T_{0thickness}$ equals $1.1 \cdot 10^{-19}$ m^3, and $n_{0thickness}$ equals $8.25 \cdot 10^{-5}$ m. The fault is considered with transverse and longitudinal properties being the same. This method guarantees that the lower-dimensional fracture elements are connected to the porous matrix elements, which represent the fault zone. By employing fully-implicit time-stepping with PorousFlow's complete Jacobian, we enhance numerical performance (Permann et al., 2020). The mechanical properties are incorporated directly into the fault zone, while the thermal-hydraulics are accounted for within both the zero-thickness elements and the fault zone. Other properties of the fault zone are chosen to match the reservoir.

The model's initial temperature is set at 134 °C, based on a calculated gradient of 35 °C/km and a surface temperature of 15 °C. Considering that the center of the reservoir is located at a depth of −3.4 km. This temperature is uniformly applied throughout the model, as depicted in Fig. 3. All the thermal boundary conditions are fixed at 134 °C. The hydraulic initial condition is characterized by a hydrostatic pressure gradient, ranging from 30 MPa at the top to 38 MPa at the bottom, with the boundary conditions maintaining this gradient.

The initial vertical (Z-direction) stress at the top of the domain is set as σ_{zz} = 75 MPa, corresponding to a 3 km overburden with a density of 2500 kg/m^3. The initial stress σ_{zz}, exhibits a gradient of 25 MPa/km across the entire domain. The initial major horizontal stress (Y-direction) is the intermediate stress, set as σ_{yy} = 61.5 MPa at the top, with a gradient of 20.5 MPa/km depth. The initial stress in the X-direction is the minor stress σ_{xx}, which is set at 52.5 MPa at the top, with a stress gradient of 17.3 MPa/km along the Z-direction. This latter value was determined via elastic theory $\sigma'_{hmin}/\sigma'_v = \sigma'_{xx}/\sigma'_{zz} = (\nu/(1-\nu))$ (Eaton, 1969), therefore not considering tectonic changes, and is therefore suitable only for exploratory analyses. The mechanical top boundary condition is defined by σ_{zz} = 75 MPa, and the bottom boundary condition is set to having no normal displacement in the Z-direction and is free to move in the other directions. The Y- and X-direction boundary conditions are also set to have no normal displacement and are free in the other directions (see Fig. 3).

Table 1
Thermal, hydraulic and mechanical properties of the rock. Properties are based on Buijze et al. (2023).

Parameters	Unit	Reservoir	Confining layer	Fault zone
Rock properties				
Biot coefficient (α_b)	–	1	1	1
Young modulus (E)	GPa	Table 3	Table 3	Table 3
Poisson's ratio (ν)	–	0.33	0.3	0.3
Density (ρ_r)	kg/m^3	2500	2500	2500
Porosity (n)	%	25	20	75
Permeability (k)	m^2	10^{-13}	10^{-19}	10^{-13}
Thermal conductivity (λ)	W/(m K)	2.5	2.5	2.5
Specific heat capacity (C_r)	J/(kg K)	1200	1200	1200
Linear thermal expansion coefficient (α_{rl})	–	$3 \cdot 10^{-5}$	$3 \cdot 10^{-5}$	$3 \cdot 10^{-5}$
Cohesion (c)	MPa	–	–	0
Friction angle (ϕ)	°	–	–	30
Dilation angle (ψ)	°	–	–	2

Table 2
Fluid properties of the model. Properties from International Association for the Properties of Water and Steam (Wagner and Pruß, 2002).

Parameters	
Density (ρ_f)	1000 kg/m^3
Viscosity (μ_f)	10^{-9} MPa s
Bulk modulus (K_f)	2 GPa
Thermal conductivity (λ_f)	0.6 W/(m K)
Linear thermal expansion coefficient (α_{fl})	$2.14 \cdot 10^{-4}$ (K^{-1})
Specific heat capacity (C_f)	4000 (J/kg K)

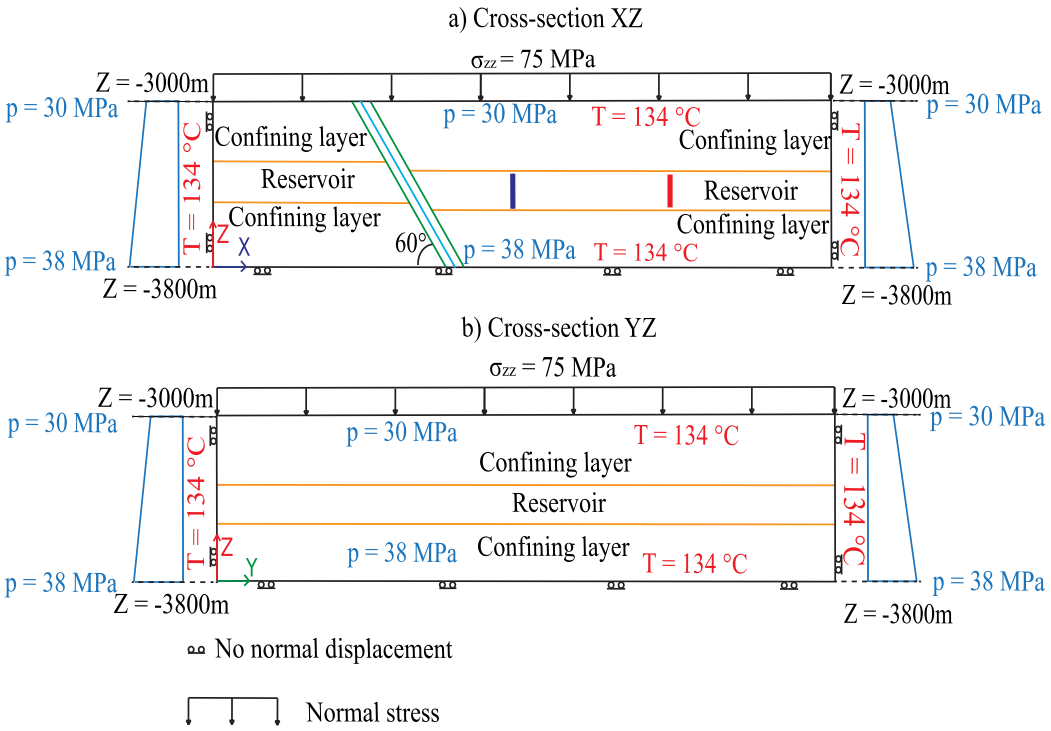

Fig. 3. Boundary conditions of the model (locations of the cross-sections refer to Fig. 2 at the center-point of the Y and X axes of the domain, respectively): (a) Cross-section XZ, (b) Cross-section YZ.

Table 3
Parameters of the different scenarios modeled. Properties are based on Buijze et al. Buijze et al. (2023).

Scenario	E_{Fault}	$E_{Reservoir}$	E_{Conf}
1	4 MPa	7 MPa	20 MPa
2	7 MPa	7 MPa	20 MPa
3	4 MPa	20 MPa	7 MPa
4	7 MPa	20 MPa	7 MPa

In this configuration, the stress regime on the fault is characterized as a normal fault (Zoback et al., 2003; Jaeger et al., 2009). A normal fault regime is typical in many deep geothermal projects, such as the GroßSchönebeck (DE), Essen (DE), Poeldijk (NL) and de Lier (NL) (Moeck et al., 2009; Buijze et al., 2019).

The model is assumed to be fully saturated and gravity is taken into account. However, changes in fluid properties, which depend on water pressure and temperature are not incorporated into the model, with the fixed values found in Table 2. This was chosen as the details of, for example, bouyancy driven flow are though to be of secondary importance for fault reactivation. Changes in fault permeability due to the evolution of aperture are not modeled. The model used 171 820 nodes and 972 427 tetrahedral elements. The mesh has been refined at the locations of the wells, on the fault and between the fault and the injection well, as shown in Fig. 4. Prior to injection, the model is in hydraulic, thermal and mechanical equilibrium. Variations in (comparative) stiffnesses were investigated, as shown in Table 3. These values are typical for Dutch projects (Buijze et al., 2023).

2.4. Slip tendency

Slip tendency is a quantification of how close a material is to slipping. It is defined as the ratio of shear stress to normal effective stress (Morris et al., 1996). This equation is a linearized Mohr–Coulomb relationship, i.e., not taking into account any cohesion, which can be defined as:

$$ST = \frac{\tau}{\sigma_n'} \leq tan(\phi) \tag{10}$$

where τ is the shear stress acting on the fault, σ_n' the normal effective stress acting on the fault and ϕ the friction angle.

If the slip tendency ratio is equal to $tan(\phi)$, and the fault does not have cohesion, then the fault is considered to be slipping. Here, a friction angle of 30° has been assumed to be indicative of a typical fault (Healy et al., 1984; Zoback, 2010).

2.5. Limitations

It is important to note that the transition from fault slippage to seismic activity is not accounted for. To achieve this, calculating the seismic moment tensor and employing more advanced constitutive models are necessary. These models would allow for the accumulation of strain energy, which could be released during specific events, leading to an uncertain frequency or magnitude of such occurrences. Additionally, incorporating changes in fluid properties with temperature would improve the accuracy of the scenarios, particularly for site-specific analyses. However, the simulations presented here depict a hypothetical geothermal exploitation scenario, and have been simplified to enhance the interpretation.

3. Results

In a uniform elastic medium, thermo-elastic stress predominantly relies on the Young's modulus and the linear thermal expansion coefficient, coupled with temperature changes (Soltanzadeh and Hawkes, 2009a,b). Hence, the investigation is made with different Young's moduli for the fault zone, reservoir and confining layers (see Table 3). This choice aims to explore how varying stiffness affects stress variation and the ruptured area of the fault within a nonhomogeneous thermo-poro-elasto-plastic model.

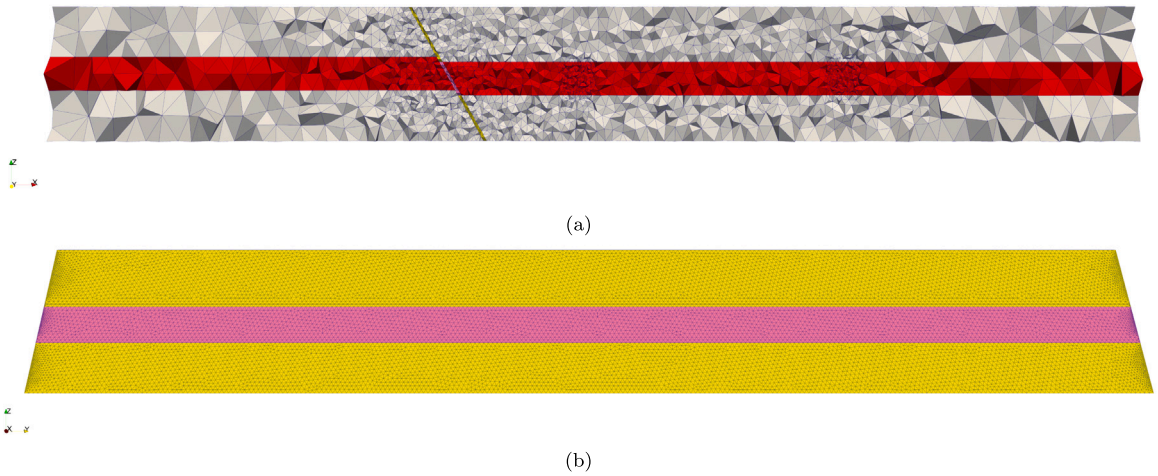

Fig. 4. Nodes and meshes: (a) Reservoir cross section, (b) Fault.

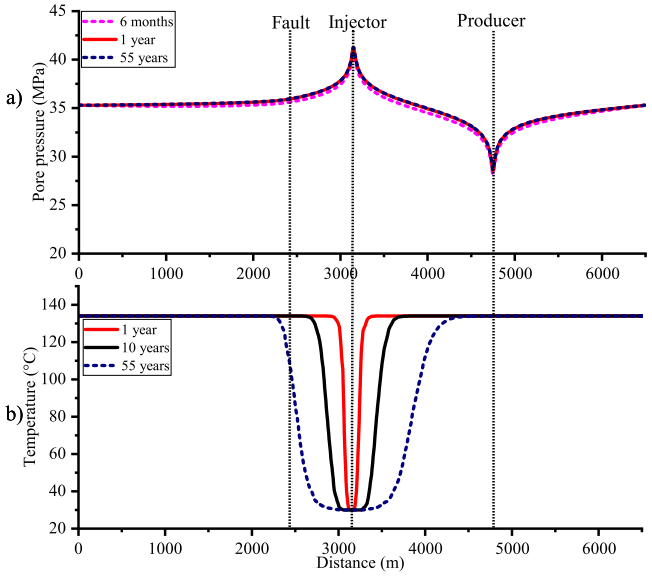

Fig. 5. Distribution inside the reservoir of (a) Pore pressure, (b) Temperature. Distance is along the scan line in Fig. 2.

3.1. Reservoir pore pressure and temperature

Cold water injection and water extraction significantly influence the pore pressure and temperature fields within the reservoir. In Fig. 5, the evolution of pore pressure and temperature in the reservoir along the scan line of Fig. 2 over different time intervals is presented. As fluid circulates, the pore pressure increases near the injector and decreases near the producer, stabilizing after one year. The pore pressure profile at 1 year and 55 years is virtually identical, indicating that the system reaches equilibrium after a year of injection. Although minor changes in pore pressure might continue if permeability is assumed to change with porosity, the overall effect of injection and extraction is a stable pore pressure distribution over time. This highlights the system's tendency to equilibrate, with long-term stability in pore pressure despite the initial perturbations (see Fig. 5)a.

The non-linear pore pressure spatial gradients are due to the radial flow away and towards the wells. The magnitude of variation in pore pressure at the wells aligns consistently with on-site measurements from Dutch geothermal projects, as documented by Buijze et al. (2023).

As fluid circulates, the temperature around the injector decreases. Fig. 5b illustrates the temperature variation within the model at different time intervals. Initially, when at rest, the temperature is at 134 °C. As fluid circulates, the temperature around the injector decreases. After 1 year, the temperature immediately around the injector drops to 30 °C, with a cooling diameter of approximately 500 m. After 10 years, the cooling radius extends to 1230 m. The cooling front makes direct contact with the fault after 27.5 years of production. By the 55th year, the diameter reaches approximately 2415 m. The cooling front advances more rapidly towards the producer (right side of the figure) compared to the injector, seen most clearly in the later stages of the analysis. The current design does not have thermal breakthrough in the investigated time.

3.2. Stress changes within the reservoir

The perturbation of pore pressure and temperature impacts the fault stress field, with varying effects depending on the reservoir stiffness. As shown in Fig. 6, stress around the injection wells decreases, while stress near the production wells increases, although to a smaller degree. In stiffer reservoirs, stress redistribution leads to greater destressing around the injection site. The horizontal stress perturbation is more elliptical, with the most significant reservoir distress occurring along the x-axis than the z-axis (see Fig. 6). These findings highlight the importance of reservoir stiffness in influencing the stress distribution and fault behavior during injection and production processes.

3.3. Stress changes at the fault

The changes in the stress field within the reservoir have a direct impact on the local fault stress. The local changes in temperature, pore pressure, and stress are depicted in Fig. 7. The evolution of pore pressure and temperature at the center point of the fault is depicted in Fig. 7a. The pore pressure exhibits a stabilization after one year of injection (from 35.3 MPa to 36.06 MPa).

The temperature of the fault (see Fig. 7a) begins at an initial temperature of 134 °C. After around 27.5 years of injection, the cold front reaches the fault, causing the temperature to sharply decrease. The smooth, but accelerating, reduction in temperature is due to the thermal conductivity reducing the severity of the thermal front. After 49.13 years of production, the initial patch undergoes reactivation, coinciding with a temperature of 117.5 °C at that time. Upon completion of the simulation, the center of the fault's temperature has reduced to 110 °C.

The contrasting behaviors highlight the critical role of stiffness. Higher reservoir stiffness increases fault reactivation and increases the

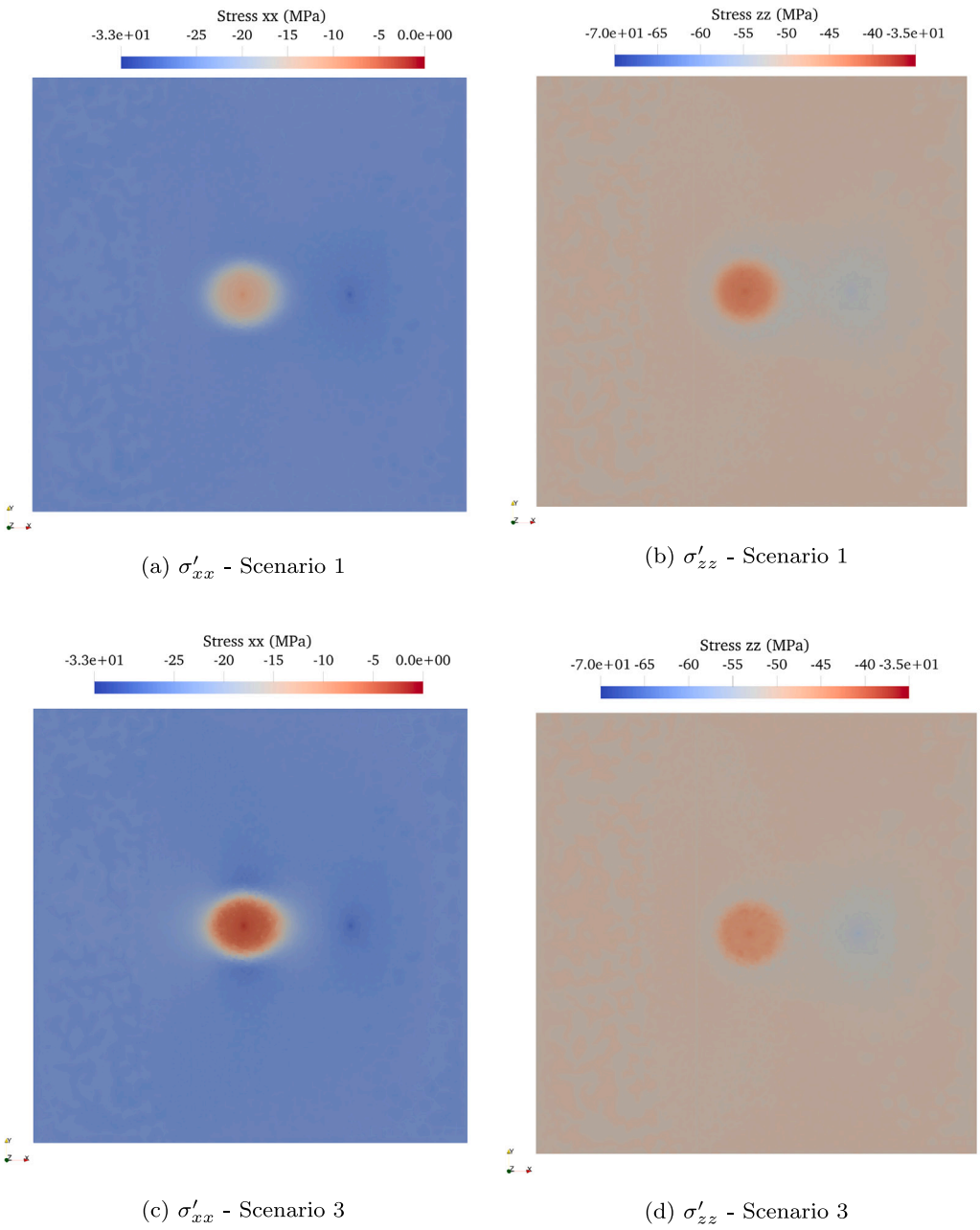

Fig. 6. Plan view of stresses at the center of the reservoir after 27.5 years of injection (a) σ'_{xx} - Scenario 1 (b) σ'_{zz} - Scenario 1 (c) σ'_{xx} - Scenario 3 (d) σ'_{zz} - Scenario 3.

rate of tangential stress accumulation (as shown in Fig. 7). Cooling further accelerates failure in Scenarios 3 and 4, demonstrating that thermal effects can significantly alter fault stability when coupled with poroelastic stress changes. The tangential shear stress acting on the fault evolves due to the interplay between cooling, pore pressure changes, and stiffness. As shown in Fig. 7b, the initial shear stress on the fault is 11.5 MPa. Over time, the stress evolution varies significantly between scenarios. In Scenarios 1 and 2, the shear stress increases throughout the simulation, reaching 13.38 MPa and 13.56 MPa, respectively, after 55 years of injection. The larger fault stiffness in Scenario 2 leads to a higher rate of stress increase compared to Scenario 1. In contrast, Scenarios 3 and 4 show fault failure due to cooling effects and lower stiffness. Scenario 3 reaches a peak stress of 14.73 MPa after 51.2 years, while Scenario 4 reaches 14.85 MPa after 49 years. Post-failure, both scenarios exhibit a reduction in stress due to stress redistribution and sliding along the failure plane.

The observed variations underscore the impact of material stiffness. Lower reservoir stiffness amplifies stress redistribution, accelerating fault instability. Conversely, stiffer confining layer exhibit more gradual stress changes, delaying fault reactivation. Effective normal stress, which governs fault stability, is also influenced by pore pressure and temperature changes (Fig. 7c). Initially, the normal effective stress is 32.5 MPa, but injection-induced changes vary across scenarios. In Scenarios 1 and 2, effective normal stress reduces and then increases slightly during the first 27.5 years due to poroelastic effects, reaching 32.1 MPa, before decreasing to 29.8 MPa after 55 years as cooling effects dominate. In Scenarios 3 and 4, the normal effective stress decreases steadily to 29.61 MPa and 29.43 MPa, respectively, after 27.5 years, and further declines to 25.31 MPa and 24.97 MPa at the end of the simulation. Cooling fronts and stiffness contrasts exacerbate stress reduction, leading to earlier reactivation in these scenarios.

Slip tendency results indicate that systems with lower confining layer stiffness are more prone to instability, due to the clamping effect

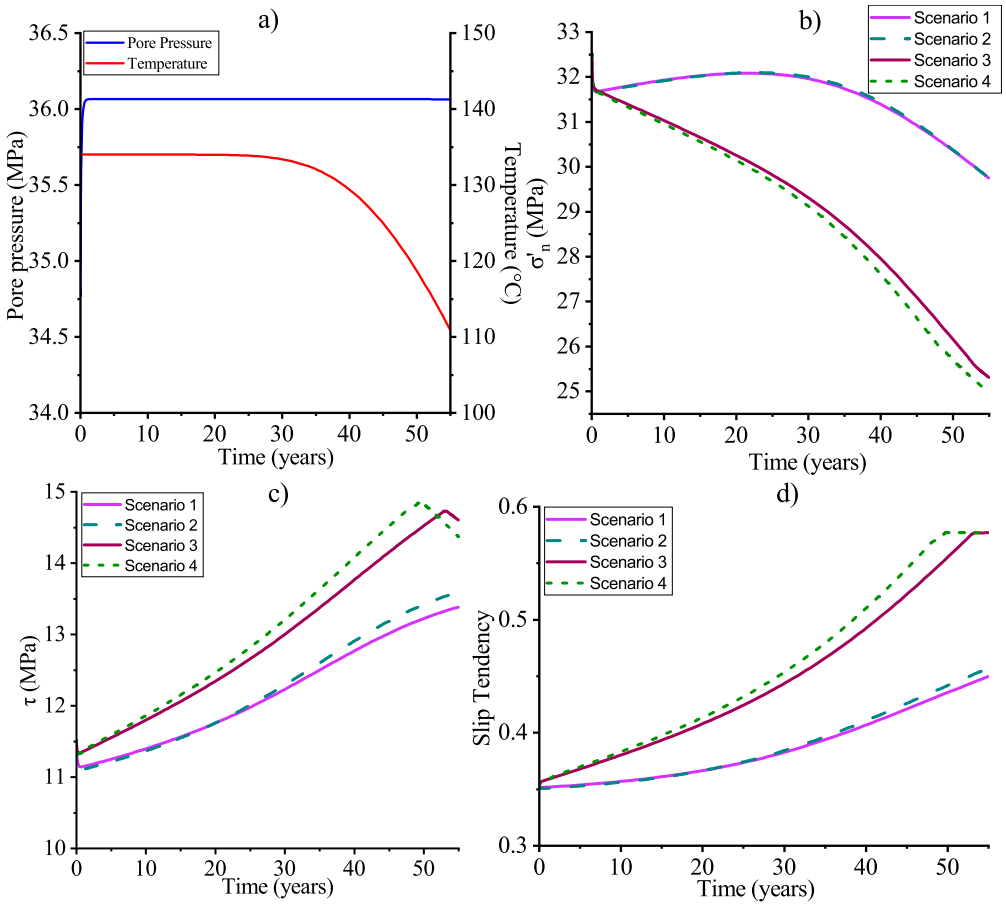

Fig. 7. (a) Temperature and pore pressure at middle of the fault (b) Tangential shear stress acting on the middle of the (c) Normal effective stress acting on the middle of the fault (d) Fault Slip Tendency Evolution.

of the confining layer. Monitoring slip tendency evolution can serve as an early warning for fault reactivation during geothermal operations. Slip tendency, defined as the ratio of tangential shear stress to effective normal stress, evolves with injection and cooling (Fig. 7d). In Scenarios 1 and 2, the slip tendency increases gradually, reaching 0.445 and 0.457 after 55 years. Faults remain stable throughout the simulation due to limited reductions in effective normal stress and moderate increases in shear stress. In Scenarios 3 and 4, slip tendency increases monotonically, eventually reaching the critical value of 0.577. Failure occurs at 51.2 years in Scenario 3 and 49 years in Scenario 4. The acceleration of slip tendency is driven by the combined effects of cooling and reduced stiffness, which amplify stress perturbations.

Poroelastic effects lead to reductions in minor stress, while cooling causes further expansion of the Mohr's circle, particularly affecting minor stress as explained in Fig. 1b. These effects, combined with changes in stress distributions, ultimately lead to fault reactivation in scenarios 3 and 4, as the minor stress reaches critical levels required for failure. During different stress perturbation regimes in the reservoir, fault stress experiences significant changes. Figs. 8a and 8b illustrate the stress state at the center of the fault at a depth of Z = -3470 m for Scenarios 1 and 2, where the Mohr's circle initially shows major and minor stresses. As fluid is extracted and injected, the Mohr's circle moves laterally without changing size due to increased fluid pressure, which isotropically affects the effective stress. However, due to the poroelastic effect and horizontal movement restrictions, the circle reduces in size. Cooling further causes the Mohr's circle to expand due to volumetric changes restrained by horizontal stress within the reservoir. The effects of stress perturbations over time vary across different scenarios. After 1 year, the major and minor stresses decrease, with Scenario 1 showing a larger decrease in the major stress compared to Scenario 2 as shown in 8a and b. After 27.5 years, both scenarios show a decrease in minor stress, but the major stress increases in both cases. At the end of the simulation, further cooling leads to a substantial reduction in minor stress, while the major stress remains largely unchanged. The stiffness of the reservoir and confining layer plays a key role in how stress is distributed. In Scenarios 3 and 4, the poroelastic effect has a lower impact on major stress due to the lower stiffness of the overburden, leading to less stress arching. After 1 year of production, both scenarios show a decrease in minor and major stresses, with Scenario 4 showing slightly larger reductions than Scenario 3. Over time, the cooling process increases the diameter of the Mohr's circle, primarily affecting minor stress as the volume of cooled rock expands. As the fault reaches the failure line, the Mohr's circle slides along it, perturbing both major and minor stresses. By the end of the simulation, further changes in stress are observed, with a notable decrease in both major and minor stresses in both scenarios as shown in Fig. 8.

Slip tendency evolves over time due to variations in pore pressure and temperature, leading to different spatial distributions across the fault depending on the stiffness scenarios. Initially, the slip tendency is uniform along the fault, but after 27.5 years of operation, areas at the top and bottom of the fault show increased slip tendency, indicating reduced stability (see Fig. 9). In contrast, the central section remains stable until the cold front reaches it. Over the course of the 55 year simulation, the instability in the central and outer sections of the fault continues to evolve, with the fault becoming progressively more unstable, particularly in the middle section, where the cold plume impacts the fault. These changes highlight how fault stability is influenced by thermal and pressure perturbations, with significant variations between the different stiffness scenarios as shown in Fig. 9.

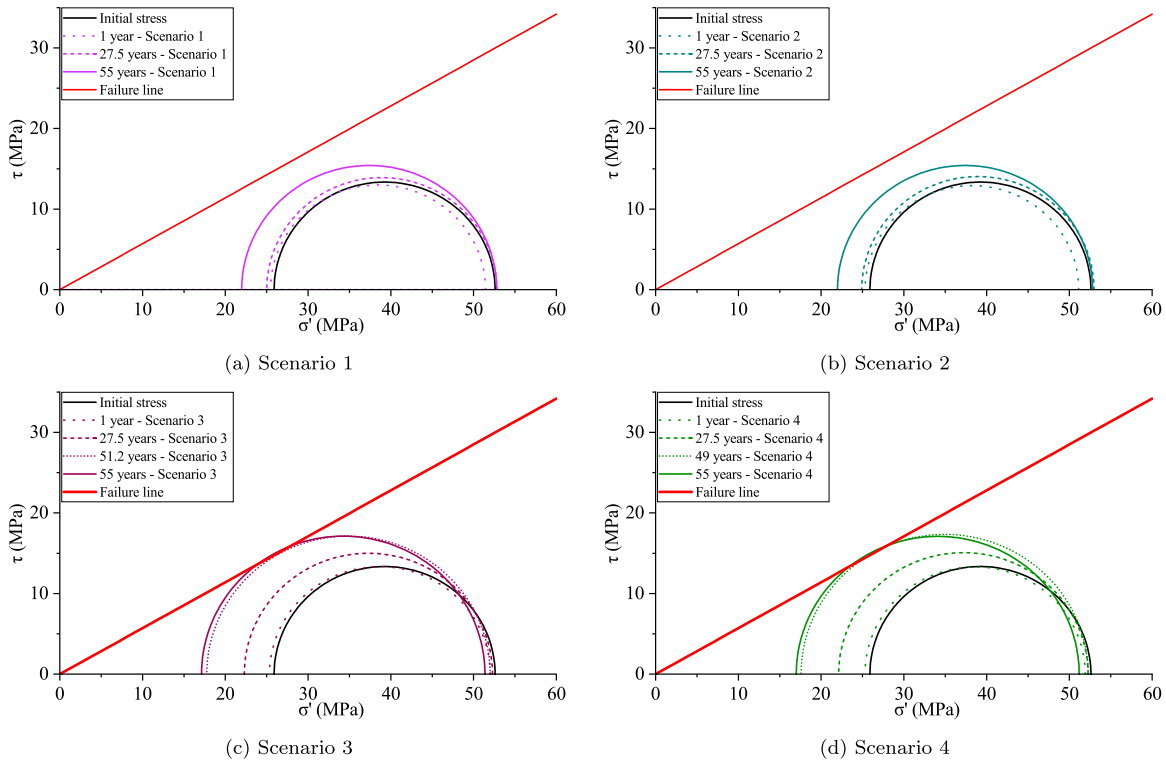

Fig. 8. Representation of effective stress evolution at the middle of the fault at Z = -3470 m with Mohr's Circles; (a) Scenario 1, (b) Scenario 2, (c) Scenario 3, (d) Scenario 4.

Fig. 10 illustrates the evolution of the ruptured area of the fault over time for different stiffness scenarios. Reactivation occurs at different points for scenarios 3 and 4, with scenario 4 showing reactivation at 49 years and scenario 3 at 51.2 years. Both exhibit a bi-linear evolution of the ruptured area over time, with inflection points at 50.8 years for scenario 3 and 53.75 years for scenario 4. Scenario 4 experiences a much larger maximum ruptured area compared to scenario 3, indicating a greater degree of fault reactivation under higher stiffness conditions. These findings highlight the sensitivity of fault reactivation to changes in stiffness, with scenario 4 being more prone to significant ruptures. This value for the ruptured area aligns with findings from other studies on fault reactivation during geothermal operations (Boyet et al., 2023; Kruszewski et al., 2023). Specifically, Boyet et al. (2023) reported a ruptured area ranging from 846 to 14236 m^2, while Kruszewski et al. (2023) observed values between 8000 and 22000 m^2.

It is seen that the stiffness of the fault results in small changes in the re-activation time, and then a stiffer fault (scenario 4) results in a slower progression of the rupture area - the rate being approximately 50% lower.

4. Discussion

4.1. Fault reactivation

Over time, it is observed that different mechanisms contribute to fault reactivation:

- Mechanism 1: Poroelastic response following injection causes the reservoir to expand, resulting in fault contraction.
- Mechanism 2: Changes in water circulation affect pore pressure due to injection.
- Mechanism 3: Reservoir cooling induces reservoir contraction, thereby causing fault expansion.
- Mechanism 4: Cold fronts percolating the fault perturb the stress regime in the fault.

These mechanisms have different dominance over time. Mechanisms 1 and 2 disturbed the stress regime early in the models, while mechanisms 3 and 4 disturbed it more significantly later in the models. The observation that pore pressure stabilizes on a monthly scale while fault reactivation occurs after several years of production indicates that the primary mechanisms driving reactivation are cooling and the percolation of cold fronts (Mechanisms 3 and 4).

The contrast in confining layer and reservoir stiffness plays a key role into how local the horizontal stress changes in the reservoir and confining layers are, and therefore also in the fault where these layers are intersected. When the reservoir is cooled, a thermally induced shrinkage occurs, and due to the overall horizontal constraint (i.e. at the model boundaries), the horizontal stress reduces. In scenarios 1 and 2, the stiff confining layer ensures that the stress changes are more local and do not propagate throughout the reservoir. In scenarios 3 and 4, the stiff reservoir is less easily constrained by the confining layers and the reduction in horizontal stress is able to more easily spread through the domain. This stress change also impacts the confining layers (both due to cooling and the mechanical interaction in other parts of the domain). The fault stiffness plays a secondary role in the resulting slip tendency, with a stiffer fault zone leading to slightly delayed fault reactivation and a higher variation of values across the fault.

4.2. Hazards

As mentioned in Section 2.5, the focus of this work is on fault rupture, and not the translation into seismicity, although fault rupture is a prerequisite for seismicity. It is seen here that in projects with similar geological conditions and fault strengths (Buijze et al., 2019), the relative stiffness of the caprock and reservoir play an important role. In situations with a stiffer caprock, the likelihood of reactivation is lower leading to a generally safer situation. However, stress changes are more local (when the cold front reaches the fault), which can reduce the potential to monitor small scale seismicity prior to significant seismicity. In situations with a stiffer reservoir, the likelihood of seismicity

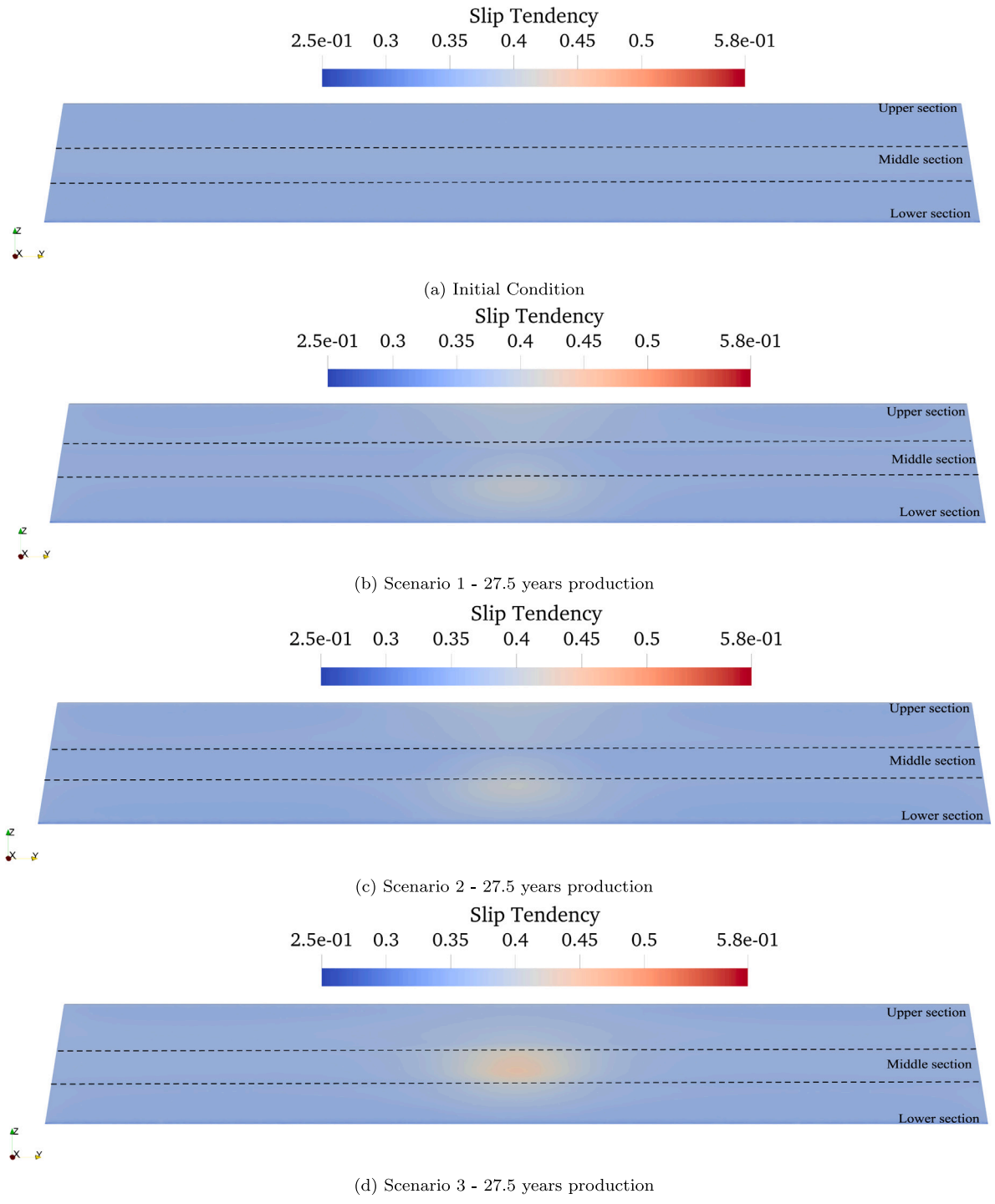

Fig. 9. Fault slip tendency: (a) Initial Condition (b) Scenario 1–27.5 years production (c) Scenario 2–27.5 years production (d) Scenario 3–27.5 years production (e) Scenario 4–27.5 years production (f) Scenario 1–55 years production (g) Scenario 2–55 years production (h) Scenario 3–55 years production (i) Scenario 4–55 years production.

is higher, but stress changes are more gradual, linked more to the overall cooling in the system. This implies that seismicity is likely to slowly increase (linked also to the predicted increase of rupture area in this work), and therefore monitoring can be used more effectively as a control tool. Reactivation is seen in this case to occur over a time span of several years. Any seismic impact will vary depending on whether the fault slip occurs incrementally or occurs in a single event and depends on several aspects including the material behavior and state. This requires further research, linking fault slip and thermo-mechanical state and behavior to the manifestation of seismicity. It is important to consider that, over a longer simulation period, the rupture area will continue to expand in the scenarios where it ruptures. Faults (or fault zones) with higher rigidity were shown to exhibit a larger slip area compared to a fault with lower rigidity (see Fig. 10). However, faults are in most cases avoided during drilling, which means that properties are difficult to estimate. This is the case in the examples considered here. This uncertainty is likely to persist in many projects and should be accounted for when assessing the temporal variation of fault rupture.

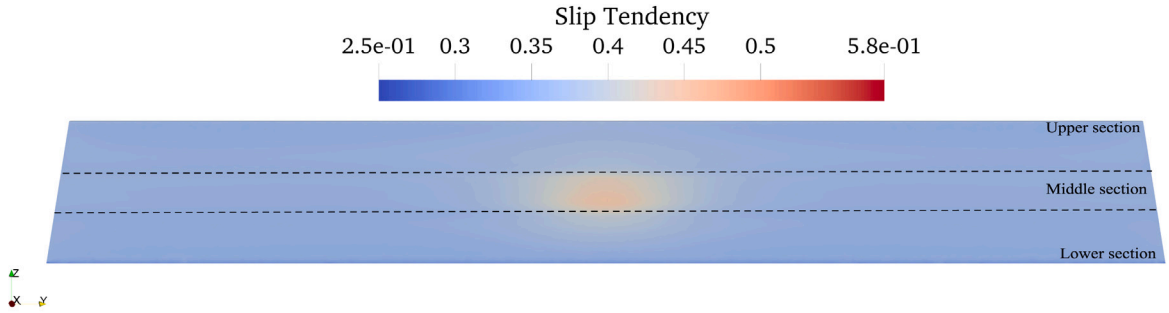

(e) Scenario 4 - 27.5 years production

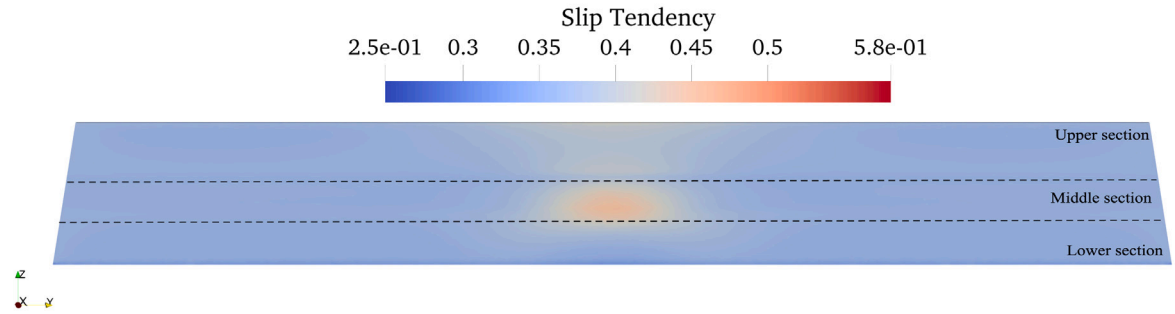

(f) Scenario 1 - 55 years production

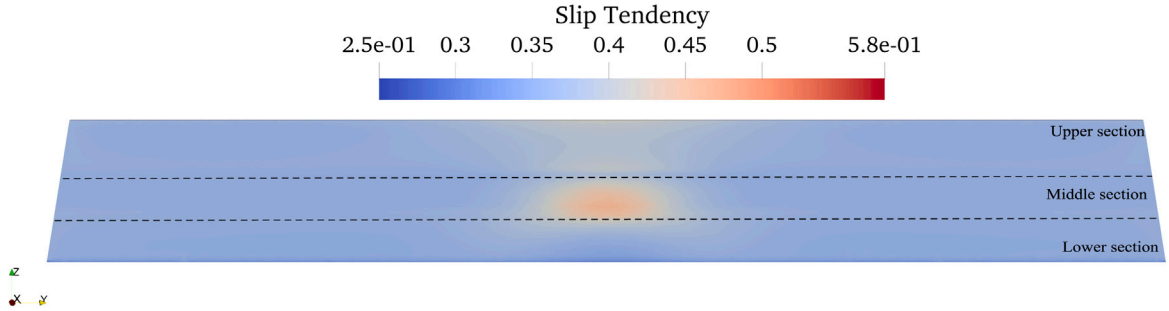

(g) Scenario 2 - 55 years production

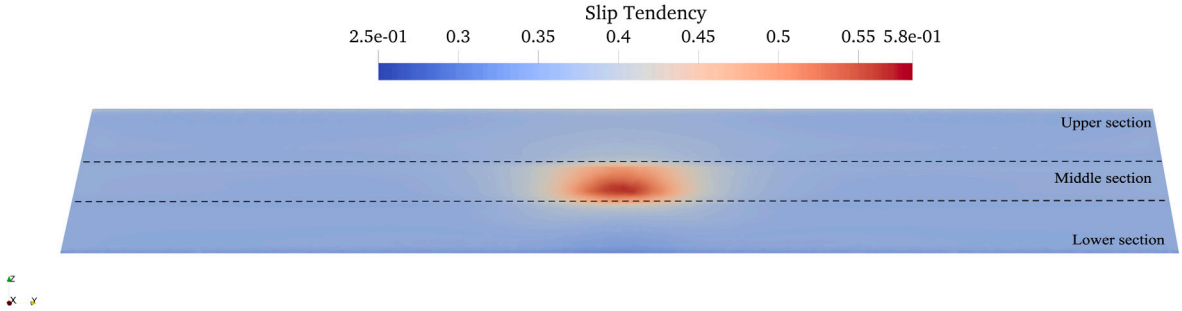

(h) Scenario 3 - 55 years production

Fig. 9. (*continued*).

5. Summary and conclusion

Understanding the reactivation of faults is crucial for mitigating the risks associated with induced or triggered seismicity in geothermal projects. A key aspect of this concern involves the cooling-induced reactivation of faults. In this study, a coupled thermo-hydro-mechanical model is presented to investigate the reactivation of faults within a porous and permeable sandstone reservoir. This work contributes to expanding our understanding of far-field fault reactivation and the impact of material properties on fault behavior. The fault under consideration was situated at 750 m away from the injection well, as is commonly targeted in hydrothermal systems. The reactivation of the fault occurs more readily in a reservoir with greater stiffness compared to the caprock.

The normal stress on the fault in this situation is seen to progressively decrease and the shear stress progressively increase. After an initial reactivation, the affected area then expands laterally due to differences in permeability and stiffness between the caprock and the reservoir. In scenarios with a stiffer caprock, the stress changes are seen to be more local to the cooling zone, and the changes progress in a more non-linear manner. In this situation, with the fault was less stable, rupture was not seen to occur. This analysis of varying stiffness provides valuable insights into how fault rigidity influences reactivation behavior, which is crucial information for geothermal development.

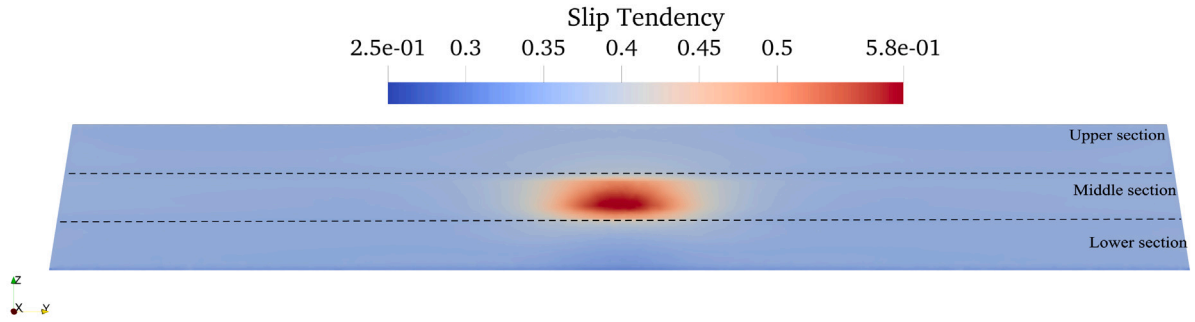

(i) Scenario 4 - 55 years production

Fig. 9. (*continued*).

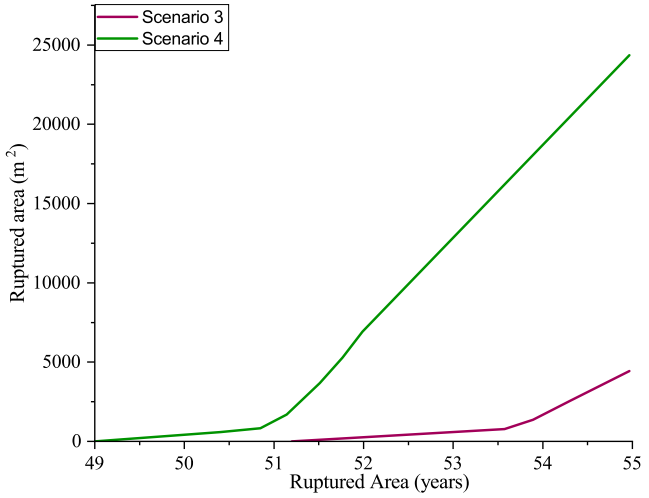

Fig. 10. Ruptured area of the fault for different fault stiffness.

In Unterhaching, Germany (Megies and Wassermann, 2014), Poing, Germany (Seithel et al., 2019) and the Californië geothermal field in the Netherlands (Voros and Baisch, 2022), fault reactivation was primarily attributed to cooling effects rather than pore pressure changes, as seismic activity was observed well after pore pressure had stabilized. Our model supports this conclusion, showing that Mechanisms 1 and 2, which reach their maximum destabilizing effect after one year of production, are not the predominant factors. Instead, cooling appears to be the primary driver of significant changes in critical slip tendency.

It is common practice to ensure that the cooling plume has limited interaction with faults, as they are considered prone to reactivation if they fall within the cooling radius. In this study, the model results partially confirm this criterion. However, it is demonstrated that the escalation of shear stress and reduction in effective normal stress are consequences of coupled mechanisms, and interactions between the caprock and the reservoir. Consequently, if the initial slip tendency value approaches its failure threshold, the fault may slip due to reservoir contraction, prior or after cold front interaction with the fault. Therefore, consideration should be given to faults that lie both inside and outside the cooling radius, especially where the caprock has a lower stiffness than the reservoir.

CRediT authorship contribution statement

Josselin Ouf: Writing – review & editing, Writing – original draft, Visualization, Methodology, Investigation, Formal analysis, Data curation, Conceptualization. **Philip J. Vardon:** Writing – review & editing, Supervision, Methodology, Funding acquisition, Formal analysis, Conceptualization. **Kavan Khaledi:** Visualization, Methodology, Investigation, Formal analysis, Data curation, Conceptualization. **Wen Luo:** Writing – review & editing, Methodology, Investigation. **Mohammadreza Jalali:** Writing – review & editing, Supervision, Methodology, Investigation. **Florian Amann:** Writing – review & editing, Supervision, Methodology, Investigation, Funding acquisition, Formal analysis, Conceptualization.

Declaration of Generative AI and AI-assisted technologies in the writing process

During the preparation of this work, the authors used Chat GPT - 3.5 in order to improve the text quality and readability. After using this tool/service, the authors reviewed and edited the content as needed and take full responsibility for the content of the publication.

Declaration of competing interest

The authors declare that they have no known competing financial interests or personal relationships that could have appeared to influence the work reported in this paper.

Acknowledgments

This work is provided under the framework of Efficiency & Safety in Geothermal Operations (EASY-GO) within the IDEA League network. We acknowledging the European Union's Horizon 2020 research and innovation program under the Marie Sklodowska-Curie grant agreement No 956965 for providing funds for the study. We also thanks two anonymous reviewers for their helpful reviews.

Data availability

Data will be made available on request.

References

Balay, S., Abhyankar, S., Adams, M., Brown, J., Brune, P., Buschelman, K., Dalcin, L., Eijkhout, V., Gropp, W., Kaushik, D., et al., 2017. PETSc users manual revision 3.8. Tech. rep., Office of Scientific and Technical Information (OSTI).

Biot, M., 1955. Theory of elasticity and consolidation for a porous anisotropic solid. J. Appl. Phys. 26 (2), 182–185.

Blöcher, G., Cacace, M., Jacquey, A.B., Zang, A., Heidbach, O., Hofmann, H., Kluge, C., Zimmermann, G., 2018. Evaluating micro-seismic events triggered by reservoir operations at the geothermal site of Groß Schönebeck (Germany). Rock Mech. Rock Eng. 51, 3265–3279.

Boyet, A., De Simone, S., Ge, S., Vilarrasa, V., 2023. Poroelastic stress relaxation, slip stress transfer and friction weakening controlled post-injection seismicity at the Basel Enhanced Geothermal System. Commun. Earth Environ. 4 (1), 104.

Buijze, L., van Bijsterveldt, L., Cremer, H., Paap, B., Veldkamp, H., Wassing, B.B.T., Van Wees, J.-D., van Yperen, G.C.N., ter Heege, J.H., Jaarsma, B., 2019. Review of induced seismicity in geothermal systems worldwide and implications for geothermal systems in the Netherlands. Neth. J. Geosci. 98, e13.

Buijze, L., Veldkamp, H., Wassing, B., 2023. Comparison of hydrocarbon and geothermal energy production in the Netherlands: reservoir characteristics, pressure and temperature changes, and implications for fault reactivation. Neth. J. Geosci. 102, e7.
Cacace, M., Jacquey, A.B., 2017. Flexible parallel implicit modelling of coupled thermal–hydraulic–mechanical processes in fractured rocks. Solid Earth 8 (5), 921–941.
Cathles, L., 1977. An analysis of the cooling of intrusives by ground-water convection which includes boiling. Econ. Geol. 72 (5), 804–826.
Cathles III, L.M., 1990. Scales and effects of fluid flow in the upper crust. Science 248 (4953), 323–329.
Chilingarian, G., Wolf, K., 1975. Compaction of Coarse-Grained Sediments, I. Elsevier.
Cryer, C.W.A., 1963. A comparison of the three-dimensional consolidation theories of Biot and Terzaghi. Quart. J. Mech. Appl. Math. 16 (4), 401–412.
Dake, L.P., 1983. Fundamentals of Reservoir Engineering. Elsevier.
Darcy, H., 1856. Les fontaines publiques de la ville de Dijon: exposition et application des principes à suivre et des formules à employer dans les questions de distribution d'eau. vol. 1, Victor dalmont.
Duboeuf, L., De Barros, L., Kakurina, M., Guglielmi, Y., Cappa, F., Valley, B., 2021. Aseismic deformations perturb the stress state and trigger induced seismicity during injection experiments. Geophys. J. Int. 224 (2), 1464–1475.
Eaton, B.A., 1969. Fracture gradient prediction and its application in oilfield operations. J. Pet. Technol. 21 (10), 1353–1360.
Geertsma, J., 1957a. The effect of fluid pressure decline on volumetric changes of porous rocks. Trans. AIME 210 (01), 331–340.
Geertsma, J., 1957b. A remark on the analogy between thermoelasticity and the elasticity of saturated porous media. J. Mech. Phys. Solids 6 (1), 13–16.
Gischig, V.S., Preisig, G., 2015. Hydro-fracturing versus hydro-shearing: A critical assessment of two distinct reservoir stimulation mechanisms. In: ISRM Congress. ISRM.
Grasselli, G., Lisjak, A., Mahabadi, O., Tatone, B., 2015. Influence of pre-existing discontinuities and bedding planes on hydraulic fracturing initiation. Eur. J. Environ. Civ. Eng. 19 (5), 580–597.
Healy, J.H., Hickman, S.H., Zoback, M.D., Ellis, W.L., 1984. Report on televiewer log and stress measurements in core hole USW-G1, Nevada Test Site, December 13-22, 1981. Tech. Rep., Geological Survey, Menlo Park, CA (United States); US Geological Survey.
Itasca, F., 2011. FLAC-Fast lagrangian analysis of continua, ersion. 7.0. Itasca Consulting Group Inc., Minneapolis.
Jacquey, A.B., Cacace, M., Blöcher, G., Scheck-Wenderoth, M., 2015. Numerical investigation of thermoelastic effects on fault slip tendency during injection and production of geothermal fluids. Energy Procedia 76, 311–320.
Jacquey, A.B., Cacace, M., Blöcher, G., Watanabe, N., Huenges, E., Scheck-Wenderoth, M., 2016. Thermo-poroelastic numerical modelling for enhanced geothermal system performance: Case study of the Groß Schönebeck reservoir. Tectonophysics 684, 119–130.
Jacquey, A.B., Urpi, L., Cacace, M., Blöcher, G., Zimmermann, G., Scheck-Wenderoth, M., 2018. Far field poroelastic response of geothermal reservoirs to hydraulic stimulation treatment: Theory and application at the Groß Schönebeck geothermal research facility. Int. J. Rock Mech. Min. Sci. 110, 316–327.
Jaeger, J., Cook, N., Zimmerman, R., 2009. Fundamentals of Rock Mechanics. John Wiley & Sons.
Jeanne, P., Rutqvist, J., Dobson, P.F., Walters, M., Hartline, C., Garcia, J., 2014. The impacts of mechanical stress transfers caused by hydromechanical and thermal processes on fault stability during hydraulic stimulation in a deep geothermal reservoir. Int. J. Rock Mech. Min. Sci. 72, 149–163.
Kirk, B.S., Peterson, J.W., Stogner, R.H., Carey, G.F., 2006. libMesh: a C++ library for parallel adaptive mesh refinement/coarsening simulations. Eng. Comput. 22, 237–254.
Kivi, I.R., Pujades, E., Rutqvist, J., Vilarrasa, V., 2022. Cooling-induced reactivation of distant faults during long-term geothermal energy production in hot sedimentary aquifers. Sci. Rep. 12 (1), 2065.
Kolditz, O., Bauer, S., Bilke, L., Böttcher, N., Delfs, J.-O., Fischer, T., Görke, U.J., Kalbacher, T., Kosakowski, G., McDermott, C.I., et al., 2012. OpenGeoSys: an open-source initiative for numerical simulation of thermo-hydro-mechanical/chemical (THM/C) processes in porous media. Environ. Earth Sci. 67, 589–599.
Krietsch, H., Gischig, V., Doetsch, J., Evans, K., Villiger, L., Jalali, M., Valley, B., Löw, S., Amann, F., 2020. Hydromechanical processes and their influence on the stimulation effected volume: observations from a decameter-scale hydraulic stimulation project. Solid Earth 11 (5), 1699–1729.
Kruszewski, M., Montegrossi, G., Saenger, E.H., 2023. The risk of fluid-injection-induced fault reactivation in carbonate reservoirs: an investigation of a geothermal system in the Ruhr region (Germany). Geomech. Geophys. Geo-Energy Geo-Resour. 9 (1), 38.
Lisjak, A., Mahabadi, O., Kaifosh, P., Vietor, T., Grasselli, G., 2014. A preliminary evaluation of an enhanced FDEM code as a tool to simulate hydraulic fracturing in jointed rock masses. In: ISRM EUROCK. ISRM, pp. ISRM–EUROCK.
Lord, H.W., Shulman, Y., 1967. A generalized dynamical theory of thermoelasticity. J. Mech. Phys. Solids 15 (5), 299–309.
Mandel, J., 1953. Consolidation des sols (étude mathématique). Géotechnique 3 (7), 287–299.
McClure, M., Horne, R., 2014. An investigation of stimulation mechanisms in enhanced geothermal systems. Int. J. Rock Mech. Min. Sci. 72, 242–260.
McTigue, D., 1986. Thermoelastic response of fluid-saturated porous rock. J. Geophys. Res.: Solid Earth 91 (B9), 9533–9542.
Megies, T., Wassermann, J., 2014. Microseismicity observed at a non-pressure-stimulated geothermal power plant. Geothermics 52, 36–49.
Moeck, I., Schandelmeier, H., Holl, H.-G., 2009. The stress regime in a Rotliegend reservoir of the Northeast German Basin. Int. J. Earth Sci. 98, 1643–1654.
Morris, A., Ferrill, D.A., Henderson, D.B., 1996. Slip-tendency analysis and fault reactivation. Geology 24 (3), 275–278.
Olivella, S., Gens, A., Carrera, J., Alonso, E., 1996. Numerical formulation for a simulator (code_bright) for the coupled analysis of saline media. Engineering computations 13 (7), 87–112.
Permann, C., Gaston, D., Andrš, D., Carlsen, R., Kong, F., Lindsay, A., Miller, J., Peterson, J., Slaughter, A., Stogner, R., Martineau, R., 2020. MOOSE: Enabling massively parallel multiphysics simulation. SoftwareX 11, 100430. http://dx.doi.org/10.1016/j.softx.2020.100430.
Piesnack, S., 2023. Tiefe geothermie in Deutschland 2023/24. Bundesverband Geothermie.
Pruess, K., Oldenburg, C., Moridis, G., 1999. TOUGH2 User's Guide, Version 2.0. Tech. Rep. LBNL-43134, Lawrence Berkeley National Laboratory, Berkeley CA, USA.
Rutqvist, J., 2017. An overview of TOUGH-based geomechanics models. Comput. Geosci. 108, 56–63.
Rutqvist, J., Rinaldi, A.P., Cappa, F., Moridis, G.J., 2013. Modeling of fault reactivation and induced seismicity during hydraulic fracturing of shale-gas reservoirs. J. Pet. Sci. Eng. 107, 31–44.
Rutqvist, J., Tsang, C.-F., 2002. A study of caprock hydromechanical changes associated with CO 2-injection into a brine formation. Environ. Geol. 42, 296–305.
Segall, P., Lu, S., 2015. Injection-induced seismicity: Poroelastic and earthquake nucleation effects. J. Geophys. Res.: Solid Earth 120 (7), 5082–5103.
Seithel, R., Gaucher, E., Mueller, B., Steiner, U., Kohl, T., 2019. Probability of fault reactivation in the Bavarian Molasse Basin. Geothermics 82, 81–90.
Sheldon, H.A., Wilkins, A., Green, C.P., 2021. Recovery efficiency in high-temperature aquifer thermal energy storage systems. Geothermics 96, 102173.
Skempton, A., 1954. The pore-pressure coefficients A and B. Géotechnique 4 (4), 143–147.
Smith, R.Y., Lesueur, M., Kelka, U., Poulet, T., Koehn, D., 2022. Using fractured outcrops to calculate permeability tensors: implications for geothermal fluid flow and the influence of seismic-scale faults. Geol. Mag. 159 (11–12), 2262–2278.
Soltanzadeh, H., Hawkes, C.D., 2009a. Assessing fault reactivation tendency within and surrounding porous reservoirs during fluid production or injection. Int. J. Rock Mech. Min. Sci. 46 (1), 1–7.
Soltanzadeh, H., Hawkes, C.D., 2009b. Induced poroelastic and thermoelastic stress changes within reservoirs during fluid injection and production. Porous Media: Heat Mass Transf. Transp. Mech. 27, 27–57.
Tadmor, E.B., Miller, R.E., Elliott, R.S., 2012. Continuum Mechanics and Thermodynamics: From Fundamental Concepts to Governing Equations. Cambridge University Press.
Terzaghi, K., 1943. Theoretical soil mechanics.
Voros, R., Baisch, S., 2022. Induced seismicity and seismic risk management–a showcase from the Californië geothermal field (the Netherlands). Neth. J. Geosci. 101, e15.
Wagner, W., Pruß, A., 2002. The IAPWS formulation 1995 for the thermodynamic properties of ordinary water substance for general and scientific use. J. Phys. Chem. Ref. Data 31 (2), 387–535.
Watanabe, N., Wang, W., Taron, J., Görke, U., Kolditz, O., 2012. Lower-dimensional interface elements with local enrichment: application to coupled hydro-mechanical problems in discretely fractured porous media. Internat. J. Numer. Methods Engrg. 90 (8), 1010–1034.
Wilkins, A., Green, C., Ennis-King, J., 2020. PorousFlow: a multiphysics simulation code for coupled problems in porous media. J. Open Source Softw. 5 (55), 2176. http://dx.doi.org/10.21105/joss.02176.
Wilkins, A., Green, C.P., Ennis-King, J., 2021. An open-source multiphysics simulation code for coupled problems in porous media. Comput. Geosci. 154, 104820. http://dx.doi.org/10.1016/j.cageo.2021.104820.
Wood, D.M., 2017. Geotechnical Modelling. CRC Press.
Zaal, C., Daniilidis, A., Vossepoel, F.C., 2021. Economic and fault stability analysis of geothermal field development in direct-use hydrothermal reservoirs. Geotherm. Energy 9 (1), 12.
Zimmerman, R., 1986. Compressibility of two-dimensional cavities of various shapes.
Zimmerman, R., 1990. Compressibility of sandstones.
Zoback, M., 2010. Reservoir Geomechanics. Cambridge University Press.
Zoback, M.D., Barton, C.A., Brudy, M., Castillo, D.A., Finkbeiner, T., Grollimund, B.R., Moos, D.B., Peska, P.L., Ward, C.D., Wiprut, D.J., 2003. Determination of stress orientation and magnitude in deep wells. Int. J. Rock Mech. Min. Sci. 40 (7–8), 1049–1076.